Computational Fluid Dynamics Methods Used in the Development of the Space Launch System Liftoff and Transition Lineloads Databases

Nalin A. Ratnayake*, Steven E. Krist, Ph.D.*, Farhad Ghaffari[†], and Karen A. Deere*
NASA Langley Research Center, Hampton, VA, 23681-2199

The objective of this paper is to document the reasoning and trade studies that supported the selection of appropriate tools for constructing aerodynamic lineload databases for the Liftoff and Transition phases of flight for launch vehicles. These decisions were made amid the maturation of an evolving workflow for generating databases on variants of the Space Launch System launch vehicle, with most being based on results from brief developmental studies performed in response to specific, unforeseen challenges that were encountered in analyzing a given configuration. This report is intended to provide a summary of the results and the decision-making processes chronologically over the design cycles of various configurations, starting with isolated free-air bodies for the Block 1 Crew, then the Block 1B Crew and Cargo configurations, and most recently the Block 1B Crew configuration in proximity to the launch tower. The results from these analyses led to the selection of the CREATE-AV Kestrel flow solver for simulating these problems. The need to accurately capture the expected leeward-wake flow-field characteristics required the use of Delayed Detached Eddy Simulation (DDES) method, for which the vorticity magnitude was employed as the solution Adaptive Mesh Refinement (AMR) function over the off-body Cartesian grid region. In addition, the Spalart-Allmaras (SA) model is used to account for the flow turbulence effects.

Nomenclature

$14x22$	=	NASA Langley Research Center 14- by 22-Foot Subsonic Tunnel
AMR	=	Adaptive Mesh Refinement
CFD	=	Computational Fluid Dynamics
$CREATE - AV$	=	Computational Research and Engineering Acquisition Tools and Environment, Air Vehicles
DAC	=	Design and Analysis Cycle
$DDES$	=	Delayed Detached Eddy Simulation
DES	=	Detached Eddy Simulation
$DFROM$	=	Data-Fused Reduced-Order Model
DoE	=	Design of Experiments
GNC	=	Guidance, Navigation, and Control
$HPCMP$	=	High-Performance Computing Modernization Program
$LaRC$	=	Langley Research Center
LAS	=	Launch Abort System
LES	=	Large Eddy Simulation
LOT	=	Liftoff and Transition (phase of flight)
$MPCV$	=	Multi-Purpose Crew Vehicle
$MSFC$	=	Marshall Space Flight Center
$NASA$	=	National Aeronautics and Space Administration
$RANS$	=	Reynolds-Averaged Navier-Stokes
ROM	=	Reduced-Order Model
SA	=	Spalart-Allmaras (turbulence model)
SLS	=	Space Launch System
SRB	=	Solid Rocket Booster

---

*Research Aerospace Engineer, Configuration Aerodynamics Branch, AIAA Senior Member
[†]Research Aerospace Engineer, Configuration Aerodynamics Branch, AIAA Associate Fellow

Variables

C_A = axial force coefficient
C_{LL} = rolling moment coefficient
C_{LM} = pitching moment coefficient
C_{LN} = yawing moment coefficient
C_N = normal force coefficient
C_P = pressure coefficient
C_Y = side force coefficient
M_∞ = freestream Mach Number
α_P, α_T = total angle of attack (missile axis system), deg
Δ = cell size, in
ϕ_P, ϕ_A = aerodynamic roll angle (missile axis system), deg

I. Introduction

The NASA Space Launch System (SLS) is comprised of a family of advanced launch vehicles designed to provide a new capability for deep-space exploration. Variants of the SLS launch vehicle consist of a common, multistage core that includes the liquid-fueled main rocket engines, with two five-segment Solid Rocket Boosters (SRBs) attached to the sides. For the SLS-10000 (Block 1 Crew) and SLS-28000 (Block 1B Crew) series, the Orion Multi-Purpose Crew Vehicle (MPCV) sits atop the stack. The Launch Abort System (LAS) is a shroud that covers the MPCV, and the LAS tower extends above it. For the SLS-27000 (Block 1B cargo) variant, the MPCV/LAS is replaced with a payload enclosed within a shroud. Fig. 1 shows the three configurations of interest in the present study and, in addition, depicts the Block 2 Crew and Cargo variants.
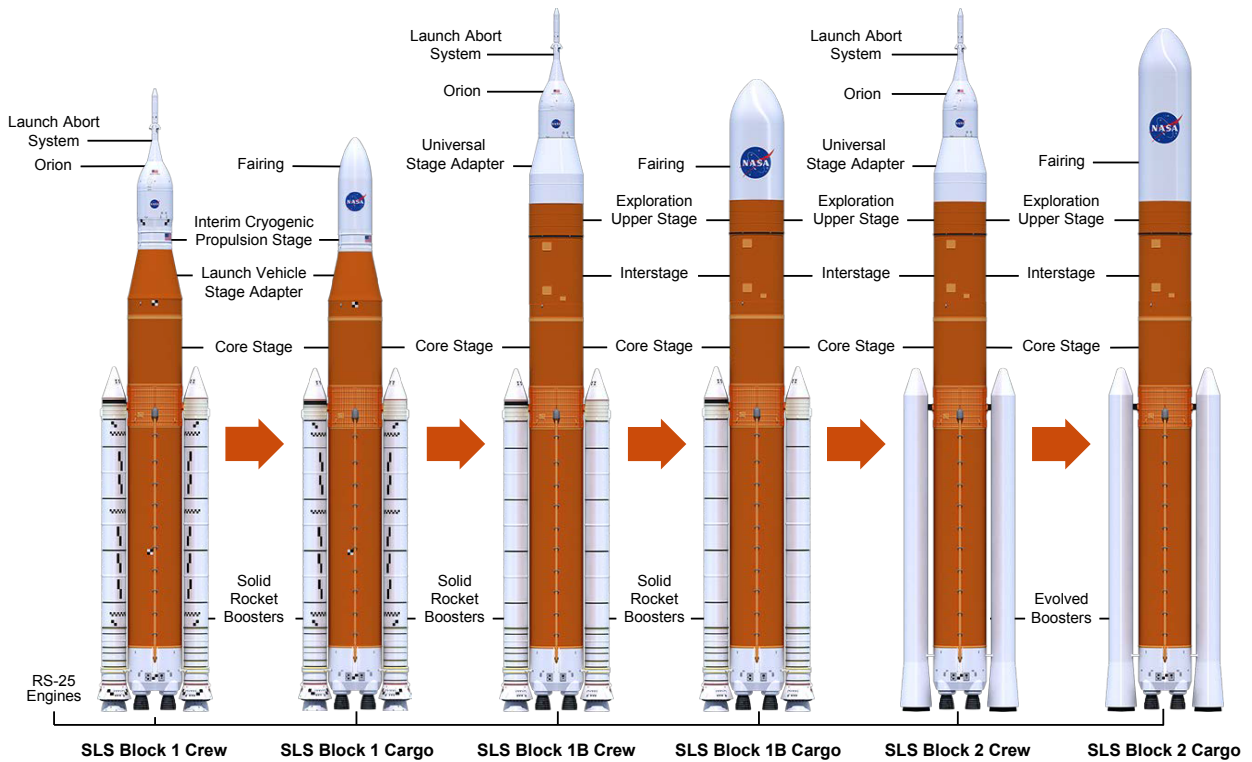

Fig. 1   SLS Vehicle Configurations.

The SLS Liftoff and Transition (LOT) Lineloads Databases provide the distributed aerodynamic forces and moments acting along the length of the various SLS configurations from vehicle on-pad, through Liftoff, then through Transition to the nominal ascent trajectory. These distributed loads are provided as a function of axial location, with individual data tables supplied for the central core stage and each of the two SRBs. The database for a configuration is comprised of two separate data sets. One dataset is for Liftoff, where significant aerodynamic interactions between the vehicle and launch tower often occur, and the other is for Transition, which covers the vehicle in isolation after it has cleared the launch tower but prior to reaching the nominal ascent phase of flight. The primary end users of the LOT Lineloads Databases are the Loads team and the Guidance, Navigation, and Control (GNC) team at the Marshall Space Flight Center (MSFC), who use the databases for sectional loading analysis and gimbal rate sensitivity analysis, respectively.

While the overall vehicle force and moment coefficients can be efficiently obtained through wind tunnel testing, computational analyses have become indispensable to obtaining the extensive amount of surface information (i.e., distributed pressure and skin friction coefficients) required to generate accurate lineloads. This paper provides a summary of the investigations conducted and decisions made by the NASA Langley Research Center (LaRC) SLS Computational Fluid Dynamics (CFD) Team in support of aerodynamic database development for the LOT phase of flight. The studies and decisions that led to the ever-evolving set of best practice procedures are documented chronologically, starting with the Block 1 Crew, followed by the Block 1B Cargo, and most recently the Block 1B Crew vehicle with and without the launch tower.

A. Aerodynamic Considerations for the LOT Problem

Aerodynamic conditions associated with the LOT regime involve low-speed flow (Mach number < 0.3) at angles of attack ranging from 0° to 90° for vehicle roll angles from 0° to 360°. In addition to such low-speed flow relative to the velocities in other SLS flight regimes, the LOT regime poses unique challenges for experimental and computational investigations due to the extreme angles of attack at various vehicle roll angles. For conditions beyond about 20° angles of attack, the flow exhibits significant leeward separation from the sides of the vehicle; the effects of the resultant large trailing wakes on the leeward surface pressure field are difficult to capture accurately in computational simulations. Moreover, a number of complex phenomena arise over the course of the Transition through the intermediary angles of attack, including the evolution of asymmetric vortex systems and the influence of Coanda effects on the flow through the gaps between the SRBs and core; both of these phenomena are extremely sensitive to small changes in orientation and geometry.

For vehicles with slender forebodies, large, stable asymmetric vortices can be generated at midrange angles of attack [2]. As illustrated in Fig. 2, the vortex on one side of the forebody will remain close to the body while the vortex on the opposite side of the symmetry plane rises away from the body, or collapses altogether. The effect of the phenomena is to induce a side force of significant magnitude on the forebody, which could appear even when the body is symmetric and/or at zero sideslip angle. Moreover, the orientation of the vortex system may switch from one side to the other on repeated instances at the same condition, as the vortex formation is extremely sensitive to minor differences in geometric features and flow conditions. Though the flow field for the asymmetric vortex system is unsteady, for most configurations the vortex pattern is stable.

None of the SLS configurations are geometrically symmetric, due to the presence of protuberances that are positioned nonuniformly over the vehicle. All variants of the SLS vehicle exhibit asymmetric vortex behavior over angles of attack ranging from roughly 20° to 70°. The orientation of the asymmetric vortex can cause not only a large change in the magnitude of the side force, but also a change in the sign. In computations, minor perturbations to parameters, such as the exact mesh geometry or solver settings, have been shown to affect the directionality of the asymmetry [3], raising the qualitative uncertainty in lateral loading. In fact, comparisons between experimental and computational results for side force will generally be quite poor unless the computation captures the same asymmetric vortex orientation as what was observed in the experiment.

Fig. 2 Asymmetric vortex formation on a cylinder at high angle of attack. Figure taken from Ref. [1].

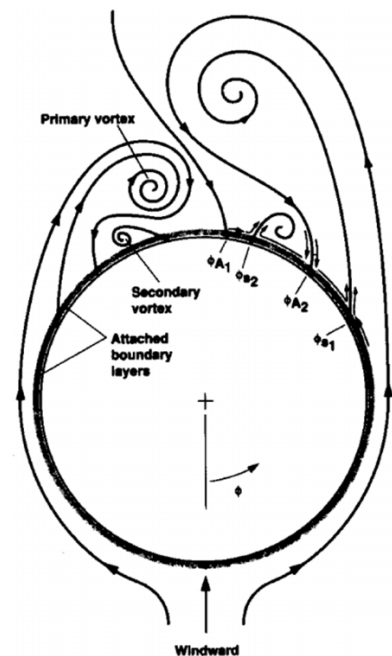Much like the situation for the asymmetric vortices, the Coanda effect exhibited in the regions around the gaps

between the SRBs and the core is extremely sensitive to geometry, flow conditions, and, in numerical simulations, the mesh geometry and flow solver parameters. The Coanda Effect has been well-characterized both analytically and experimentally in the literature and is described well by Levinsky and Yeh [4]. In the situation for the SLS vehicles in the LOT flight phase, the Coanda effect creates a tendency for the flow on the leeward side of the gaps to attach and wrap around either the core or the SRBs. If the flow wraps around the SRB, then the increased velocity generates more negative pressure coefficient values on the leeward side of the SRB and more positive values on the leeward side of the core, with the reverse being true if the flow wraps around the core. Numerical simulations of SLS configurations suggest that the Coanda effect appears at angles of attack from 15° (the lowest angle of attack for which simulations were run) through 90°.

Fig. 3 SLS Block 1B Cargo (27005) configuration wind tunnel test article shown with the launch tower model in the 14x22 Wind Tunnel.

For flow approaching the SLS vehicle from the top surface (into the page in Fig. 1), which corresponds to an angle of attack of 90° and roll angle of 0°, one can posit at least four possible Coanda modes for describing the flow in the regions around the leeward side of both gaps:

- The flow bends to the left, attaching to the port SRB and the starboard side of the core.
- The flow bends to the right, attaching to the port side of the core and the starboard SRB.
- The flow bends both SRBs.
- The flow bends both sides of the core.

The number of possible Coanda states increases when one considers that partial cases of the above are also possible. For instance, at a roll angle of 60°, the starboard SRB is upstream of the core yet still exhibits the Coanda effect, but since the port SRB lies entirely within the wake of the core, there is no significant flow through the gap between the port SRB and core. Moreover, for roll angles in the ranges around 90° and 270°, there is no significant flow through either of the gaps between the SRBs and core and, as the angle of attack approaches 0°, the Coanda effect fades away for all roll angles.

While a number of lateral loading possibilities exist for some of the flow conditions, the influence of the various Coanda modes on the magnitudes of the forces and moments is not nearly as large as that of the asymmetric vortex orientation. Nevertheless, the Coanda mode does have a significant effect on the lineloads for the SRBs and core, and it is relatively easy to discern whether a CFD result captured the same Coanda mode that was captured in the wind tunnel through comparison of the pressure coefficients at the experimental pressure tap locations.

The challenges described above are compounded for the Liftoff phase of flight, where the addition of the SLS launch tower into the flow domain gives rise to significant interference effects upon the vehicle's aerodynamic forces and moments [5]. A photograph of the Block 1B Cargo wind tunnel test article in proximity to the launch tower, installed in the NASA Langley Research Center 14- by 22-Foot Subsonic Tunnel (14x22) during Liftoff testing, is shown in Fig. 3. The launch tower apparatus is attached to a turntable so that testing can proceed through a 330° range in azimuth angle. Given the limits of the test set up, all wind tunnel testing and computations for the Liftoff phase of flight are conducted at 90° total angle of attack. Particular challenges and decisions associated with the launch tower CFD gridding and solution development are described in the companion paper by Krist, Ratnayake, and Ghaffari [6].

B. Computational Considerations for the LOT Problem

The fundamental difficulty in numerical simulations for the LOT flight regime lies in accurately capturing the effects of large wakes on the pressure field about the leeward surface of the vehicle. It has long been common knowledge in the CFD community that Reynolds-Averaged Navier-Stokes (RANS) solutions fail to accurately capture the leeward separation that initiates the formation of large wakes [7]. As the LOT regime encompasses conditions with very high angles of attack, numerical simulations of this problem demand the employment of schemes that are more complex than RANS methods. Since the application of Large Eddy Simulation (LES) methods to LOT problems remains infeasible, it is necessary to resort to hybrid RANS/LES methods, such as Detached Eddy Simulation (DES) methods and its many variants, including Delayed DES (DDES). As described by Spalart [8], DES methods essentially involve using RANS methods in the boundary layer region and LES-like methods for the extended wake. DES methods can be used with any turbulence model that makes use of a properly defined length scale. However, the computational grid must be sufficiently refined on the leeward side of the vehicle in order to adequately capture the small eddy content of the wake, making DES methods much more resource intensive than RANS methods.

Initial flow solutions to the SLS Transition problem were obtained using the Tetrahedral Unstructured Software System (TetrUSS) [9], which is developed and maintained at LaRC. The TetrUSS flow solver, USM3D, is capable of implementing RANS and DES methods on unstructured tetrahedral grids in conjunction with a variety of turbulence models. Exposure to the resource requirements of the USM3D DES simulations for the Transition problem, along with the expectation of even higher costs for the Liftoff problem, led to evaluation of the FUN3D [10] and Kestrel [11] flow solvers, both of which have the option for implementing DDES methods on unstructured mixed element grids.

Over the course of analyzing multiple SLS configurations, many challenges were encountered and overcome, leading to the selection of the following computational method and strategy:

- Flow Solver: CREATE-AV Kestrel
- Turbulence Model: DDES method coupled with the Spalart-Allmaras (SA) turbulence model
- Grid Approach: unstructured near-body grid trimmed from 24 to 36-inches, Cartesian off-body grid
- Cartesian Adaptive Mesh Refinement (AMR): adaption threshold based on vorticity magnitude

The CFD simulations reported herein have all been run on the Pleiades large Linux cluster of the NASA Advanced Supercomputing (NAS) facility located at the NASA Ames Research Center. Typical CFD solutions of the Transition problem required grids with as few as 500 million cells, whereas the Liftoff problem with the launch tower eventually utilized grids comprised of over three billion grid points. Computer resource requirements for a single run involved anywhere from 480 to 2400 Haswell processors, running anywhere from five to ten days. With such expensive resource demands, solution development efficiency at all points in the CFD workflow, from gridding to numerical simulation to post-processing, while still maintaining acceptable accuracy, was of paramount concern in the selection of tools.

C. Lineloads Database Development Workflow

In the overall workflow for generating LOT Lineloads Databases, CFD falls into an intermediary but necessary step between wind tunnel testing and creation of a mathematical Reduced-Order Model (ROM). The nominal workflow is shown in Fig. 4. In this environment, CFD is performed for a limited set of wind tunnel flow conditions determined by a Design of Experiments (DoE) study to provide the optimal subset of information in the desired lineload database space. The surface pressure and skin friction surfaces from the CFD are then passed through a ROM, which uses the modal information in the CFD solutions to generate an interpolated, multidimensional space of surfaces across all points in the desired database range. Such surfaces from the ROM can be integrated to derive lineloads at flow conditions where no CFD solutions were obtained.

In order to improve the accuracy of the model, the ROM forces and moments are anchored to wind tunnel measured data, allowing for corrections that create a Data-Fused Reduced Order Model (DFROM). The DFROM lineload coefficients as a function of body station are finally transformed into the desired coordinate system (usually body-axis) and tabulated at all desired database breakpoints. Details on the methodology and development of the ROM and DFROM are described in the companion paper by Wignall [12].

II. SLS Block 1 (10003)

The first SLS configuration for which LOT lineloads were developed was the Block 1 Crew configuration from Design and Analysis Cycle 2 (DAC2), also designated as the SLS-10003 configuration. The Outer Mold Line (OML) for the CFD model of the SLS-10003 configuration, which is quite similar to the definition for the wind tunnel model, is shown in Fig. 5. The metric portion of the vehicle, upon which integrated forces and moments are measured, includes
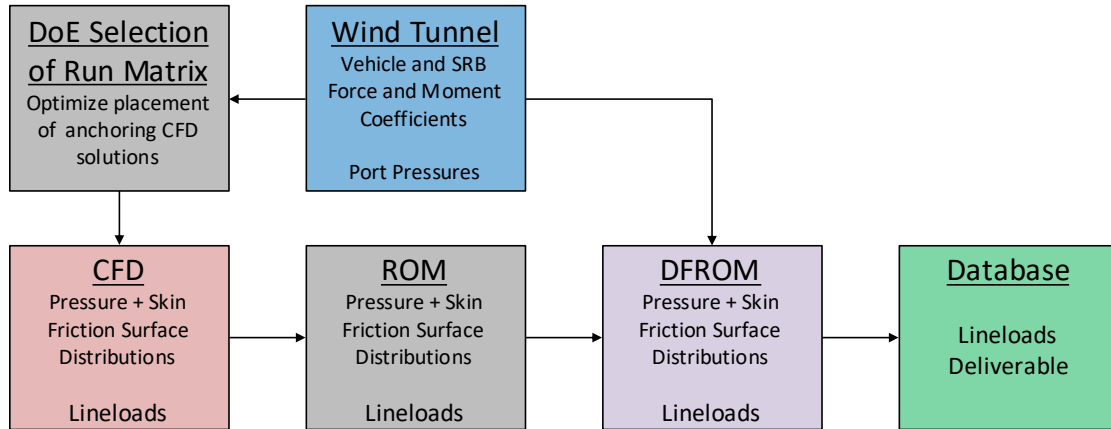
Fig. 4   High-level workflow for Liftoff/Transition Lineloads Database development.

the core stage from the top of the LAS to the termination of the nozzle aerodynamic fairings and the SRBs from the conical fairing at the top to the base of the SRB nozzles (purple and magenta surfaces). The measured forces and moments do not include the black base surfaces, the cavity, or the sting. While the model of this configuration is quite complex, it does not include many of the features included in subsequent models, such as the numerous structural support rings on the SRBs, the brackets on the feedlines, and a host of small protuberances.
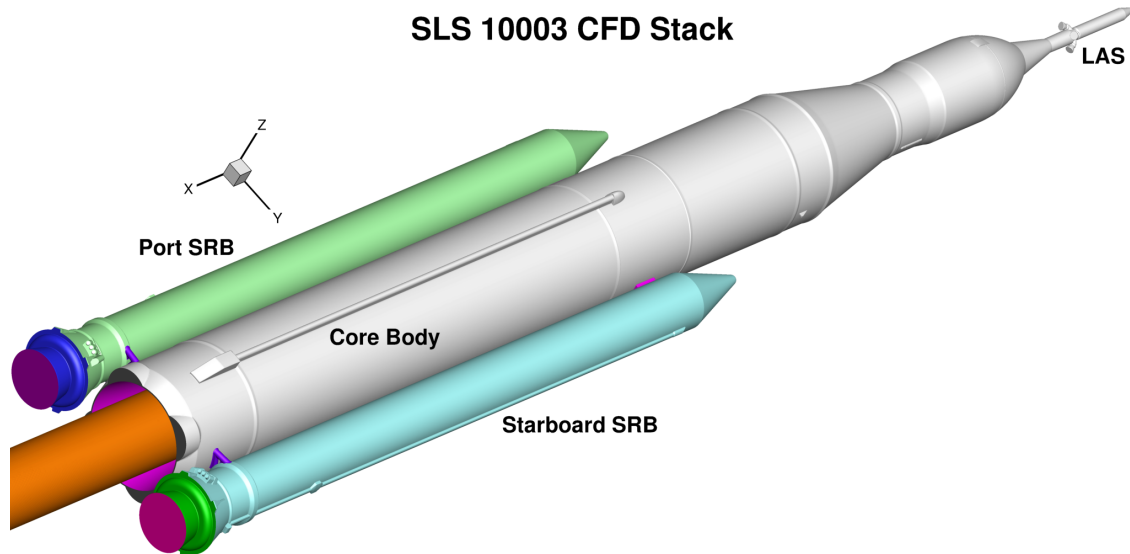

Fig. 5   OML of the SLS-10003 configuration used for CFD simulation, based on the wind tunnel model.

Due to the complexity of the SLS launch vehicle OMLs, an unstructured grid approach was chosen for the CFD analysis. Moreover, for the five years immediately preceding the SLS program, the LaRC SLS CFD Team had been using the TetrUSS suite of tools to construct aerodynamic databases for the ascent regime of the Ares-I launch vehicle as part of NASA's Constellation Program [13]. Hence, the selection of USM3D as the flow solver was a natural initial choice for this complex problem. The components of the TetrUSS software system have been applied to and validated on a wide array of aerodynamic problems over the course of roughly two decades [14]. The USM3D flow solver is a cell-centered, finite volume method for solving the Euler and Navier-Stokes equations on tetrahedral grids. In addition to the traditional RANS capability, USM3D provides an implementation of DES and supports a variety of turbulence models for closure of the Navier-Stokes equations.

6

The initial strategy used in developing the grids and setting the input parameters for USM3D was based upon the best practice procedures for analyzing the aerodynamic characteristics of the Ares-I family of launch vehicles, as documented by Abdol-Hamid and Ghaffari [15]. While these procedures are useful, they were developed for the Ascent phase of flight, which is a flow regime where RANS computations were deemed to be suitable. In order to develop practices appropriate for DES computations, prior to tackling the complexity of the SLS configuration a series of DES computations were conducted on a circular cylinder, then on a simplified Titan III configuration.

A. Titan III Studies

The Titan III commercial launch vehicle is a three-body configuration which is superficially similar to the SLS launch vehicles (see Fig. 6), making it a suitable candidate for study of interaction effects and other considerations that were unncessary for the Ares-I. Experimental force and moment data, along with limited pressure data, were available at liftoff conditions, providing validation data for the simulations. Moreover, the simplified Titan III geometry provides a much cleaner, and thus less resource intensive and time-consuming, problem than that for the SLS configurations, further bolstering the argument for using the Titan III as a test case.

Applying the best practices that were current at time, USM3D runs were set to use a second-order accurate spatial discretization with Roe's flux-difference splitting scheme for the inviscid fluxes. Since significant regions of the flow were expected to be unsteady for most of the conditions within the LOT flight envelope, all of the computations were run in time-accurate mode. The second-order time-accurate differencing scheme with the pseudotime variable was employed.

The most commonly used turbulence models in aircraft and spacecraft aerodynamic assessments are the one-equation SA model and the two-equation Menter Shear-Stress Transport (SST) model. The SA model tends to be the more robust of the two and the more widely used. Nonetheless, the SST model has been used extensively in computing jet interaction effects, where preservation of the shear layer between the freestream flow and jet plume become quite important. A third candidate is the two-equation k-ϵ model, which is often preferred when the accurate capture of free shear layers is important.

The smaller resource requirements of the Titan III problem allowed for timely investigations into refinements of the gridding procedures, the generation of temporal and spatial resolution studies, and assessment of the SA, SST, and k-ϵ turbulence models within the DES mode of

Fig. 6   A model of the Titan III in the Ames 14ft wind tunnel. Photo credit: NASA (ARC-1962-A-29073).

computations. Results from those studies indicated that RANS solutions were only adequate up to angles of attack less than 20°, and led to the selection of the k-ϵ turbulence model for simulations conducted on the SLS configuration. The studies also yielded new guidelines for gridding the SLS configuration, which are discussed below.

B. SLS-10003 Grid Development

Generation of the unstructured tetrahedral grids for USM3D was performed with the TetrUSS utilities GridTool, VGRID, and POSTGRID. The grid generation process begins with importation of the CAD geometry into GridTool, where surface patches covering the entire OML are defined, then grouped to form components. Of primary importance in generating accurate solutions is the source specification, as the grid spacing and local density of the cells will be related to the strengths and locations of the sources, thereby allowing the user to refine the grid in regions of high flow field gradients. Line sources with anisotropic stretching are typically employed at regions where components intersect or where there are sharp discontinuities in the OML surface. Volume sources in the shape of a cylinder, cone, or sphere are employed within the perimeter of the larger components of the vehicle. Output from GridTool is then imported to VGRID, which employs a three-step process to generate an unstructured volume mesh composed of tetrahedra. The first

step generates a surface triangulation, the local resolution of which is controlled by the source specification. The second step employs an advancing layer method to grow a boundary layer grid normal to the surface. The third step employs an advancing front method to discretize the inviscid flow region. The final step is to use the tool POSTGRID to close holes in the volume grid left by the VGRID process.

The only significant difference in generating grids for RANS and DES simulations is how the wake region is treated. Since no attempt is made to resolve the wake regions in the RANS simulations, all of the volume sources lie just within the OML surface. That is not the case for the DES grids, as volume sources must extend well out into the flow field on the leeward side of the vehicle in order to provide sufficiently fine resolution in the wake region. Appropriate strategies for specifying the source strengths and distributions were developed through a grid resolution study of the Titan III. Of particular importance was the determination of the representative cell size (Δ) that is to be applied to the isometric gridding of the wake. The final specification for wakes behind the various components was set such that the ratio of the nominal grid spacing to the diameter of the component was kept around 0.017; the source strengths for the volume sources in the wakes of the SRBs was set at 2.5, whereas the value for the volume source in the wake of the core stage was set at 5.5. This ratio lies toward the coarser end of the recommended spacing limits for DES studies of the circular cylinder problem. The Titan III study was also used to size the radius of the volume sources in the wakes. The spacing for the height of the first layer of cells off the wall was set at 0.01 to ensure that y+ values over the entire surface of the vehicle remained lower than 1.0; subsequent plots of y+ contours indicated that maximum values of around 0.7 were reached.

Since finely resolved regions of the off-body domain quickly drive up the resource requirements for a simulation, a separate DES grid must be generated for each roll angle in order to avoid unnecessary resolution of the flow field upstream of the vehicle. By contrast, a single RANS grid is suitable for all roll angles. The effect of skewing the volume sources in order to appropriately position the refined wake for a specified roll angle is shown in Fig. 7, where cross sections of the grid running through the core stage and SRBs is shown for the RANS grid and the DES grid for a roll angle of 60°. Note that the grid spacing from the SRB wake sources is finer than that from the core stage wake source and overrides the core stage source influence in the region of overlap.
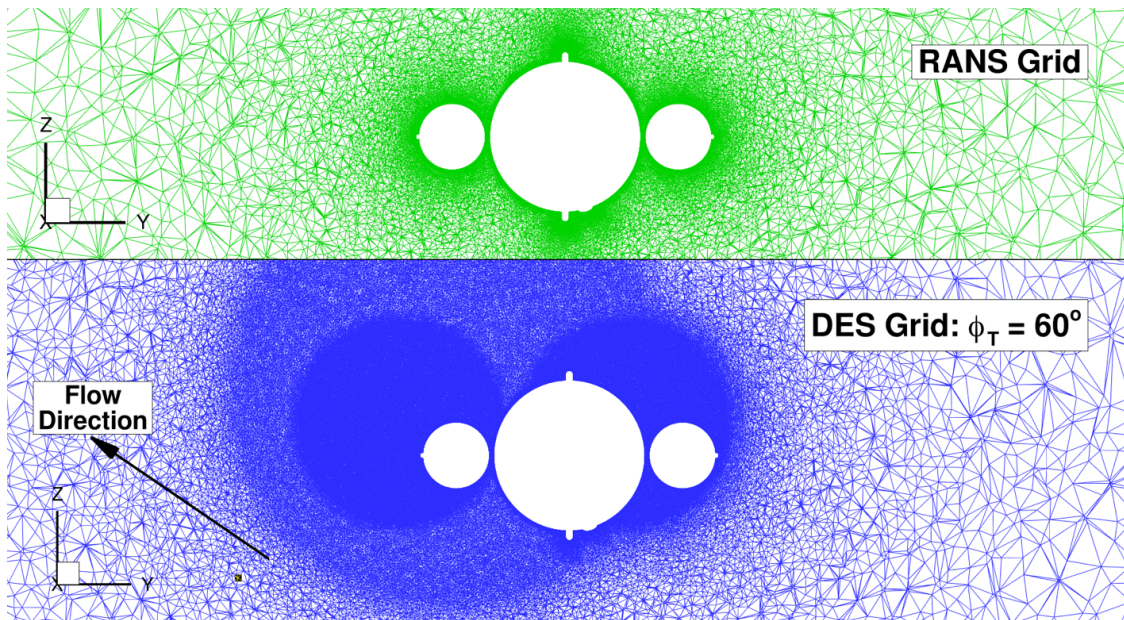

Fig. 7   Cross section of the SLS-10003 Unstructured RANS grid and the DES grid for $\phi_P = 60°$.

The RANS grid was composed of roughly 186 million cells, which makes it about 20 percent larger than the grids typically generated for ascent analyses of SLS configurations with substantially larger numbers of protuberances. The DES grids ranged from 438 million to 460 million cells, depending on the roll angle. The grids represent what would be considered a medium level of refinement in a grid study.

C. USM3D Results for SLS-10003

The approach developed from the Titan III study were applied directly to the setup for the SLS-10003 Transition problem. The run matrix was comprised of five RANS cases run at $\alpha_P = 0°$ and $10°$, and sixteen DES cases run at $\alpha_P = 30°, 55°, 70°$ and $90°$, with roll angles at $\phi_P = 0°, 30°, 60°$, and $90°$; all of the cases utilized the k-ϵ turbulence model. The computational results were obtained at wind tunnel conditions of Mach 0.183 at a Reynolds number of 615,000 based on the nominal core diameter. Note that for the full scale vehicle in the expected placard (launch safety limit) winds, the Mach number at liftoff conditions is closer to 0.05 and Reynolds number is closer to 10 million. However, M = 0.183 was the minimum speed level in the test section of the 14x22 at which acceptable data quality could be obtained. Further, present CFD methodologies are generally known to be similarly inadequate at very low speeds as well.

The solutions were run at a normalized time step of $\Delta t = 8.0$, using 10 subiterations per time step. Given a five-day limit on each supercomputer job and the typical request for 1200 processors, each run was limited to roughly 16000 time steps. Although the time dependent solutions never reach a strict definition of convergence, they do reach a point where time histories of the integrated forces and moments flatten out and the subsequent trends can be characterized as having reached a statistically-steady state, as the values oscillate about some pseudomean value. Once a statistically-steady state was reached, time averaging procedures within the code were invoked and the solutions were run for an additional 4000 time steps, thereby defining the window over which time averaged values of the force and moment coefficients and surface and volume flow properties were computed. For the SLS-10003 case, a statistically-steady state was reached at anywhere from 20000 to 40000 time steps, with the higher cases at higher angles of attack taking longest to reach that state.

Correlations between the USM3D simulation and wind tunnel results were better than was expected based on the correlations between CFD and experiment for the Titan III. An indication of the quality of results obtained with USM3D is provided in Fig. 8, where the force and moment coefficients for a pitch sweep at a roll angle of $0°$ are shown from CFD simulations and the wind tunnel force and moment database. Due to the sensitive nature of the data, magnitudes of the coefficients are not included. However, as an aid in understanding the data trends, a horizontal line is provided at the zero value of the coefficient with positive values above zero. Further, the ranges of the vertical axes for the normal and side force are the same, as are those for the pitching and yawing moment. The error bars shown on the open circles indicate the wind tunnel force and moment database uncertainty. Note the large magnitude of the error bars between $\alpha_P = 20°$ and $50°$, which reflects the scarcity of data in this region due to model dynamics issues.

Trends and magnitudes in the normal force and pitching moment, which are by far the largest coefficients at this orientation, are well captured by the CFD. Nonetheless, the coefficient values for $\alpha_P = 55°$ and above lie at the outer edge of the wind tunnel database error bar. For the side force and yawing moment coefficients, the wind tunnel values remain near zero up to $\alpha_P = 20°$, after which the values become positive, gaining significant magnitude by $\alpha_P = 40°$, then eventually decrease back to zero by $\alpha_P = 90°$. The CFD values for the lateral coefficients exhibit trends that are similar to those of the wind tunnel values, but are of opposite sign and underpredict the magnitude of the wind tunnel values. The behavior of the lateral coefficient values with increasing angle of attack is a consequence of the vortex asymmetry issue. As discussed in Sec. I.A, the directionality of the asymmetric vortices is known to be stochastic, so if the CFD captures the vortex of the opposite orientation as that which was realized in the experiment, the comparison to wind tunnel data will be poor. However, such occurrences do not necessarily indicate a flaw in the CFD result.

The other set of wind tunnel data that can be used to validate the CFD results is the static pressure data, which are taken at 150 pressure ports located on the model stack. The cross sections at which the groups of ports are located are shown in Fig. 9. An additional line of pressure ports (not shown) is taken longitudinally along the core at a clock angle of $30°$ from the y axis; for this particular view, the line of ports would appear as running down the starboard side of the core.

The view shown in Fig. 9 is of the leeward surface for the orientation at $\alpha_P = 30°$ and $\phi_P = 0°$, a condition for which the asymmetric vortex observed in the CFD has the opposite orientation as that which was captured in the wind tunnel. Red contours indicate positive pressure coefficient values, with decreasing values moving through yellow and green to blue, which indicates negative values. While the pressures appear to be largely symmetric from the nose through Station 1, by Station 2, they are distinctly asymmetric, and by Station 3, the flow is no longer symmetric at all across the Y = 0 plane.

The asymmetry is confirmed in the plot of the wind tunnel and time averaged CFD pressure coefficient data for Station 4 at $\alpha_P = 30°$ and $\phi_P = 0°$, shown in Fig. 10. In this plot, the view is looking forward; that is, the port SRB is on the left and the starboard SRB is on the right of the figure. The aerodynamic convention for plotting the pressure coefficient is employed, with the vertical axis direction reversed from the usual orientation, with higher values on the axis indicating lower pressure. The wind tunnel data are shown with the black open circles, red lines show the actual
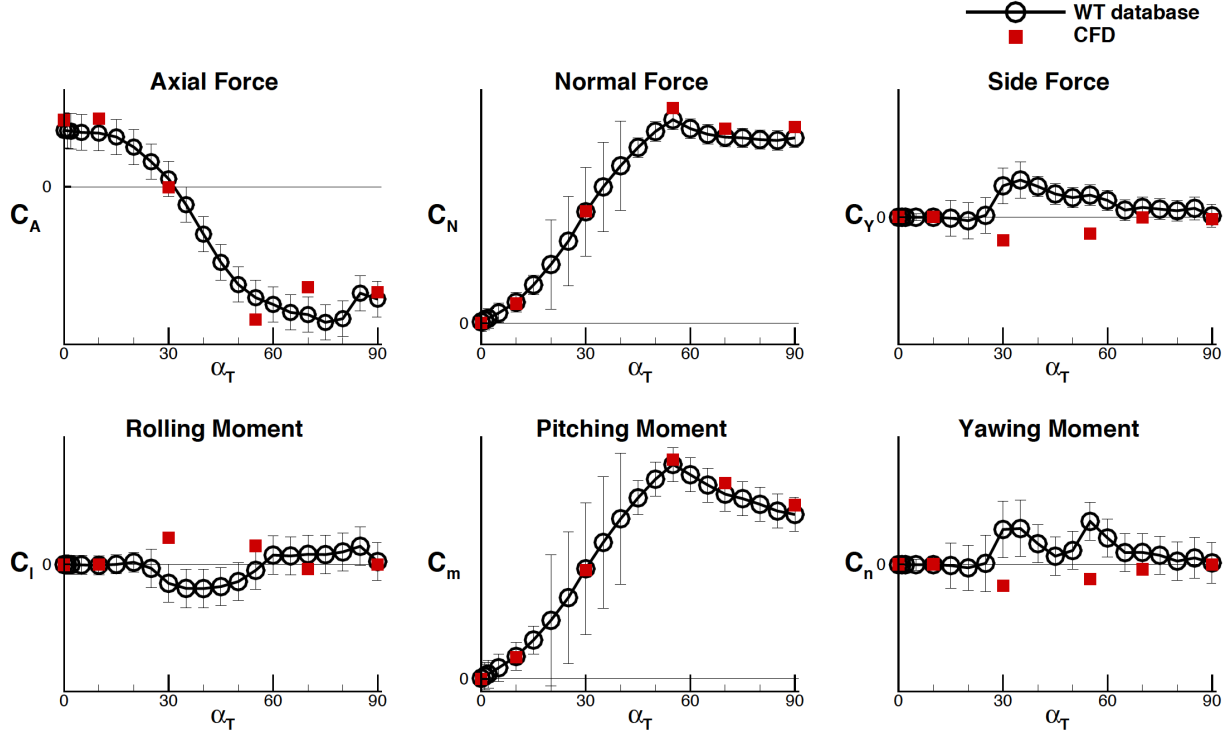
Fig. 8 **Force and moment coefficients from the wind tunnel force and moment database and DES k-ϵ results at $\phi_P = 0°$.**

CFD values, and blue lines show the CFD values plotted against the negative values of the Y coordinate, thereby giving an estimate of what the CFD pressures would have been if the CFD had captured the same orientation of the asymmetric vortex exhibited in the wind tunnel test. It is evident that the actual CFD results are poorly correlated with the wind tunnel values. However, upon reversing the Y coordinate of the CFD data, very good agreement with the wind tunnel values is obtained.

More extensive results from the initial CFD results for the SLS-10003 vehicle at Liftoff conditions were published by Krist and Ghaffari in Ref. [16], which contains additional comparisons of the CFD results to data taken from the LaRC 14x22 wind tunnel test for this configuration (Test 609).

III. Methods Refinement Following Block 1 Analysis Cycle

Prior to undertaking the job of generating databases for the two Block 1B configurations, a number of studies were initiated to improve upon the existing SLS LOT workflow. While the accuracy of the results obtained using USM3D for the Block 1 vehicle was sufficient, the enormous amount of time required for the CFD workflow (gridding + flow solving + post processing) was deemed unacceptable in the context of program schedule and the needs of end-users of the aerodynamic data products. Furthermore, USM3D did not yet support a functional implementation of the DDES method at the time, which was considered a deficiency. As shown by Spalart et al. [8] and others, inherent limitations with DES for certain classes of problems can be overcome with implementations of DDES and other variants of hybrid RANS/LES methods.

As discussed next, additional studies undertaken to try and decrease the time it took to get a solution of the LOT problem with USM3D were not particularly successful, so the decision was made to search for an alternative flow solver. The two alternative solvers that were evaluated were FUN3D and Kestrel, described in their respective subsections below. The primary reason for selecting these two flow solvers is that they utilize mixed element unstructured grids, provide existing DDES capability, and have significant support groups working constantly to keep the codes up to date in terms of both flow solver features and maximizing the speed with which they run on state of the art computer clusters.
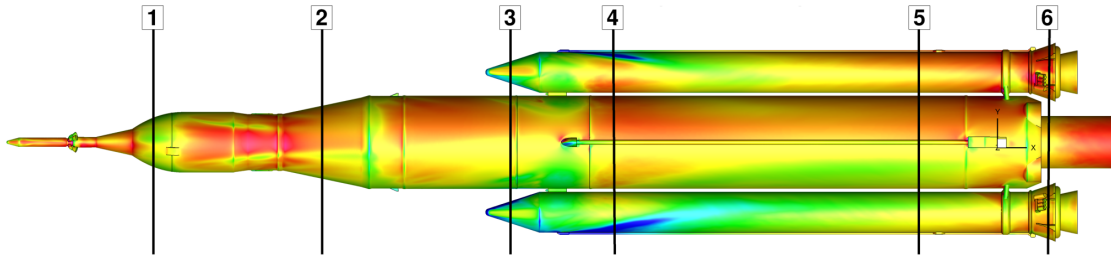
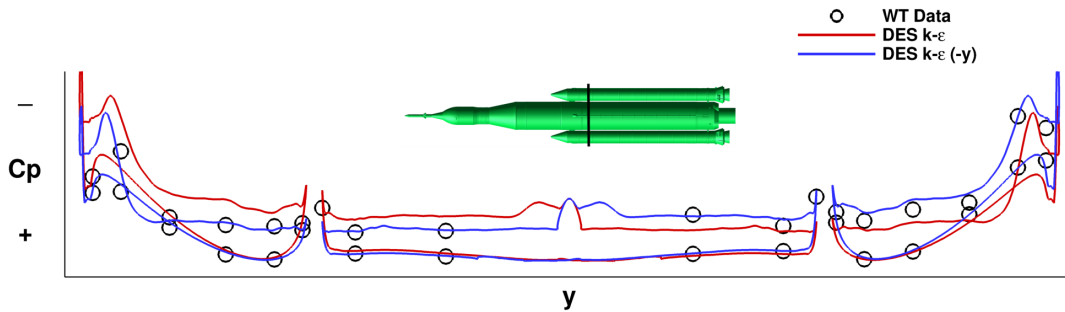**Fig. 9 Pressure coefficient on leeward surface from DES k-ϵ result at $\alpha_P = 30°$, $\phi_P = 0°$.**

Fig. 10 Pressure coefficient from wind tunnel data and DES k-ϵ results for Station 4 at $\alpha_P = 30°$, $\phi_P = 0°$ for the computed data (red) and the reversed data in the -Y coordinate (blue).

A. Additional Investigations with USM3D

One of the conclusions from the USM3D simulations for the Block 1 LOT problem was that while the cost of DES solutions was prohibitive for generating the large number of runs needed to fill out a database, the cost of RANS runs was quite reasonable. Hence, several representative cases were run with USM3D using the k-ϵ turbulence model with both the RANS and DES methods. As expected, DES provided significantly better correlation to the database force and moment values and wind tunnel surface pressure results than the RANS approach, particularly on the leeward side of the vehicle.

Since selection of the k-ϵ model over the SA and SST models was based on results from the Titan III studies, the decision was reexamined by running a series of DES simulations at roll angles of 0° on the SLS-10003 OML. The integrated force and moment results from simulations using the three turbulence models are quite similar, with the largest difference being around 8%. Likewise, there was little to distinguish between the three models in plots of the wind tunnel and CFD pressure coefficient data for the three DES simulations. Pressure coefficient plots at selected stations for the $\alpha_P = 70°$ case are shown in Fig. 11, with time-averaged results for the SA model in red, SST model in blue, and k-ϵ model in green. At Station 5, the only distinguishable difference is that on the port side (left side of the figure), the SST leeward surface pressure is less negative than for the SA and k-ϵ models; this turns out to be a consequence of the SST simulation capturing a Coanda mode that attaches to the port side of the core, while the SA and k-ϵ models capture the mode that attaches to the port SRB. Pressures along the line of ports located on the leeward side of the core stage at an orientation of $\phi = 30°$, shown in the lower portion of Fig. 11, indicate that results from the three models are in good agreement except in the region aft of Station 2. This is the region where the OML transitions from the diameter of the MPCV to that of the core, over which it is apparent that the k-ϵ model predicts a larger expansion of the flow than the SA or SST results. The anomalous behavior of the k-ϵ result can be attributed to the weakness of the model in flows with regions of large pressure gradients, although similar issues in the region did not arise at other flow conditions.

Ultimately, the team concluded that the difference in validity of the solution between the three turbulence models, as applied to the SLS 10003 configuration, was negligible. This was a surprising conclusion, since the Titan III results were very sensitive to the choice of turbulence model. It is conjectured that the improved correlation of the three models
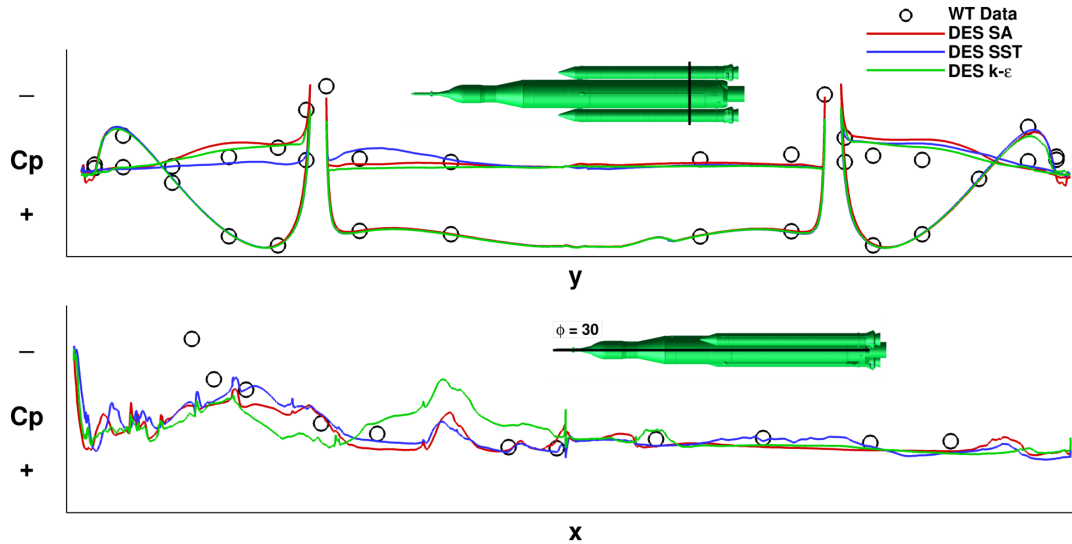
11

Fig. 11 Pressure coefficient values from Wind Tunnel Test 609 and USM3D using various turbulence models, shown for Station 5 and an axial line along the length of the vehicle at a clock angle of 30°.

on the SLS configuration is due to the influence of the protuberances on the SLS. In particular, at the 0° roll angle that was assessed, systems tunnels on the outboard sides of the SRBs are likely to fix the location of the separation at the same position for all three turbulence models, whereas the Titan III model had no protuberances at these critical locations. In the end, the study led to a preference for the SA model, since, as a one-equation model, it was more resource-efficient than the other two turbulence models.

The main deficiency in using USM3D for the LOT problem does not appear to be due to the use of DES rather than one of the more advanced DES variants, but instead that the solution simply takes too long to reach a statistically-steady state. Hence, a study was initiated in an attempt to accelerate the solution progression. The only technique that resulted in significant time savings was to run with a much larger time step (normalized $\Delta t = 40$) over the first 2000 time steps, then revert to the initial time step for the rest of the run, which yielded run times that were around two thirds that of the original runs.

B. Evaluation of FUN3D

The FUN3D flow solver is well known for its design optimization, propulsion, and thermodynamic model capabilities, with applications from incompressible flows all the way up to the hypersonic regime [10]; it is developed and maintained at LaRC. FUN3D is a node-centered method for solving the Euler and Navier-Stokes equations, in both the incompressible and compressible forms, on both standard tetrahedral grids and mixed element unstructured meshes with arbitrary combinations of tetrahedra, prisms, and pyramids. In addition to traditional RANS capability, it supports DES, DDES, and modified DDES (MDDES) methods in conjunction with a number of variants of SA and two-equation turbulence models.

In comparing the FUN3D and USM3D results, it is important to bear in mind the differences between the node-centered FUN3D solver and the cell-centered USM3D solver. For the DES grid constructed for roll angles of 0°, the computational grid contains 459 million tetrahedral cells, but only 78 million nodes. Hence the USM3D solutions have roughly six times as many degrees of freedom as FUN3D solutions on the same grid, and the representative cell size (Δ) for the wake gridding would be twice as large in the FUN3D solution as in the USM3D solution. Consequently, to obtain a direct comparison between the USM3D and FUN3D solvers, a much finer grid must be generated for the FUN3D solution. However, the grid generation code VGRID was unable to successfully generate the volume grid for grids much larger than the medium grids generated for USM3D. Hence, in generating the FUN3D grid utilized in the following comparisons, it was decided to push the VGRID process to its limit. This resulted in a grid with 717 million cells and 122 million nodes, so the number of degrees of freedom in the following FUN3D solutions is about 26% of that in the USM3D solutions.

Simulations on the SLS-10003 configuration were conducted with FUN3D version 12.7. Modeling options were

12

thoroughly exercised with runs conducted at $\alpha_P = 30°$ and $90°$ and $\phi_P = 0°$. Simulations for RANS, DDES, and MDDES were all made with the standard SA model, SA with a rotation correction (SA-R, results not included in this paper for brevity) and SA with both rotation and curvature corrections (SA-RC). Solutions with the incompressible formulation were only made with the RANS and DES methods using standard SA. The solutions were run at a normalized time step of $\Delta t = 50$ for 2000 time steps, then $\Delta t = 25$ for 2000 time steps, then, if a statistically-steady state had been reached, it was run another 4000 time steps for the time averaging window. As with USM3D, 10 subiterations per time step were used. For the SLS-10003 cases, a statistically-steady state was reached at anywhere from 4000 to 8000 time steps, with the $\alpha_P = 90°$ cases taking longest to reach that state.

One of the more interesting findings from the FUN3D results was the sensitivity of the Coanda mode to the flow solver and turbulence model. The effect is demonstrated in Fig. 12, where Mach number contours at Station 4 for the DDES SA, DDES SA-RC, and MDDES SA compressible runs at $\alpha_P = 90°$ and $\phi_P = 0°$ are shown; green contours denote the windward freestream flow on the bottom of the figure, blue denotes low-speed flow, and red denotes high-speed flow. It is clearly evident that for the DDES SA run the flow through the gaps attaches to the port SRB and starboard side of the core. However, it attaches to both sides of the core for the DDES SA-RC run, and attaches to both of the SRBs for the MDDES SA run.

Corresponding plots of the pressure coefficient data for the wind tunnel and the three simulations are shown in Fig. 13. For each of the cases, it is apparent that the most negative pressures on the leeward surfaces are associated with the corresponding flow through the gap wrapping around and attaching to a given component. Even though the DDES SA result exhibits the best correlation with the wind tunnel values, since it must have captured the same Coanda mode as observed in the wind tunnel, the other solutions are still valid, as even small changes in geometry or conditions may trip the Coanda effect into a different mode.
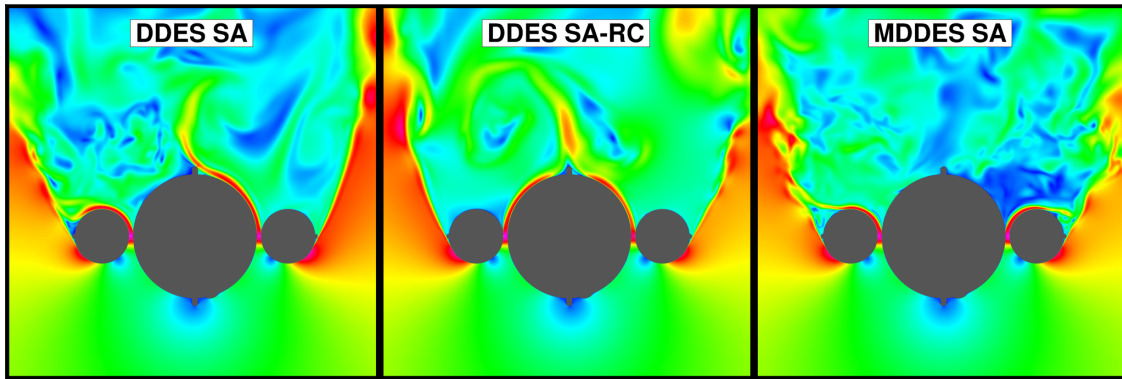

Fig. 12 Mach Contours at Station 4 for FUN3D simulations at $\alpha_P = 90°$ and $\phi_P = 0°$, using DDES SA, DDES SA-RC, and MDDES SA.
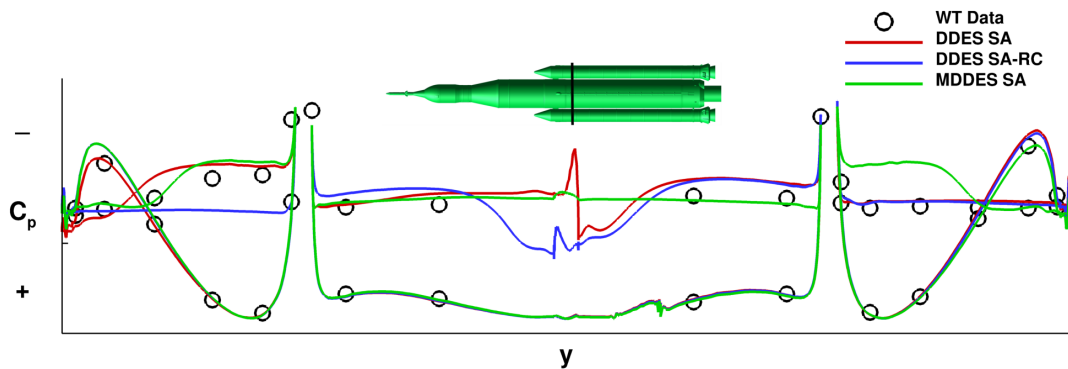

Fig. 13 Pressure coefficient at Station 4 from wind tunnel data and FUN3D simulations at $\alpha_P = 90°$, $\phi_P = 0°$.

Similar to the issue with the Coanda mode, the simulations at $\alpha_P = 30°$ were difficult to assess since the correlation with experiment was dependent on whether or not the method captured the orientation of the asymmetric vortex

13

expressed in the wind tunnel. Altogether, FUN3D simulations from 14 different combinations of turbulence model and flow solver model were completed and all of them were reasonable and similar to one another. Again, with little to distinguish the results in a meaningful way, the most straightforward conclusion was to select the compressible DDES SA method for use in grid and time step resolution studies. Of course, due to the sensitivity of the phenomena, refinements in both grid resolution and time step frequently flipped the orientation of either the asymmetric vortices, the Coanda mode, or both.

C. Evaluation of Kestrel

The Kestrel flow solver is developed and maintained by the Computational Research and Engineering Acquisition Tools and Environment, Air Vehicles (CREATE-AV) project under the US Department of Defense High-Performance Computing Modernization Program (HPCMP). The software was developed in response to a DoD need for quick-turnaround, high-fidelity analysis of complex configurations and scenarios in order to support acquisition efforts [11]. The Kestrel software utilizes a Common Scalable Infrastructure to implement a modular approach for connecting the computational tools required to conduct multidisciplinary assessments of fixed-wing aircraft. Of particular interest to the team was the fact that the architecture enables a dual mesh flow solver methodology, in which the computational domain is divided into near-body and off-body domains. The near-body flow is computed on an unstructured grid that encapsulates the solid body, and this near-body grid surrounded by a Cartesian mesh that extends to the far field. Within the overset domain, where the near-body and off-body grids overlap, hole cutting, connectivity operations, and interpolation between the two domains are handled with a python based infrastructure.

The dual mesh approach provides a significant advantage in simulating flows that contain regions of massively separated flow. In these cases, the extensive wake on the leeward side of the body can be resolved in the off-body Cartesian mesh, for which operations are significantly cheaper to implement than operations on the near-body unstructured grid. Moreover, the Cartesian mesh is much more suitable for the use of higher-order spatial discretization and is amenable to the implementation of solution Adaptive Mesh Refinement. Both of these capabilities aid in obtaining the greatest possible accuracy while running on the smallest possible grid.

The flow solver within Kestrel that is employed on the near-body domain is KCFD, a cell-centered, finite volume method for solving the Euler and RANS equations on mixed element unstructured meshes. Available turbulence models include a number of the SA variants and the Menter two-equation model with and without Shear Stress Transport. In addition to the traditional RANS capability, KCFD provides an option for DDES for use in situations involving massively separated flow. The CFD code employed on the off-body domain is SAMAir, a finite difference method for solving the Euler and RANS equations on Cartesian meshes that is derived from an earlier code, ARC3DC, developed at the NASA Ames Research Center. SAMAir is capable of implementing all of the models available in KCFD, allowing for a uniform implementation of the governing equations in both solvers.

While there are numerous Kestrel input parameters to be set for LOT simulations, the LaRC SLS CFD team was fortunate enough to have the initial input parameters set up by the lead authors of Ref. [11], namely, Scott Morton and David McDaniels. Consequently, most of the effort in exploring options for the Kestrel input parameters have been in regard to the resolution and extent of the solution adaption region for the wake. In order to illustrate some of the finer points, a cross section of a Kestrel grid generated at the end of a simulation for the Block 1 configuration at $\alpha_P = 30°$ and $\phi_P = 0°$ is shown in Fig. 14. In the main portion of the figure, the unstructured grid around the vehicle is not shown in order to clearly delineate the extent of the Cartesian grid in the vicinity of the body; the offset figure shows the overlap between the unstructured grid and the Cartesian mesh in the gap between the port SRB and the core. The position of the overlap region is dictated by the trim distance used in trimming down the unstructured grid, and the size of the grid cells at the outer edge of the unstructured grid; in this case, the trim distance is 24 inches. For reference, this trim distance is on the order of one-tenth the nominal core diameter.

The near-body unstructured grid for the Kestrel simulations was very similar to that for USM3D, as the only difference in generating the grids was with regard to the volume sources. For USM3D, the volume sources for capturing the wake needed to be manually skewed and aligned with the freestream flow direction for each roll angle, otherwise a large cost would be paid for refining the region upstream of the vehicle where nothing of interest is happening. In contrast, the Kestrel unstructured grid is trimmed to form the near-body grid only, so it is not that costly to refine upstream of the vehicle. Hence, for the Kestrel grids, the volume sources for the core and SRBs were centered on the centerline of the respective component, and one grid suffices for all roll angles. Upon generation of the grid, the Kestrel tool Carpenter was used to trim the near-body grid and merge the tetrahedral elements into mixed-elements, such as prisms and pyramids. The resulting near-body grid is on the order of 100 million cells. In comparison, over the course
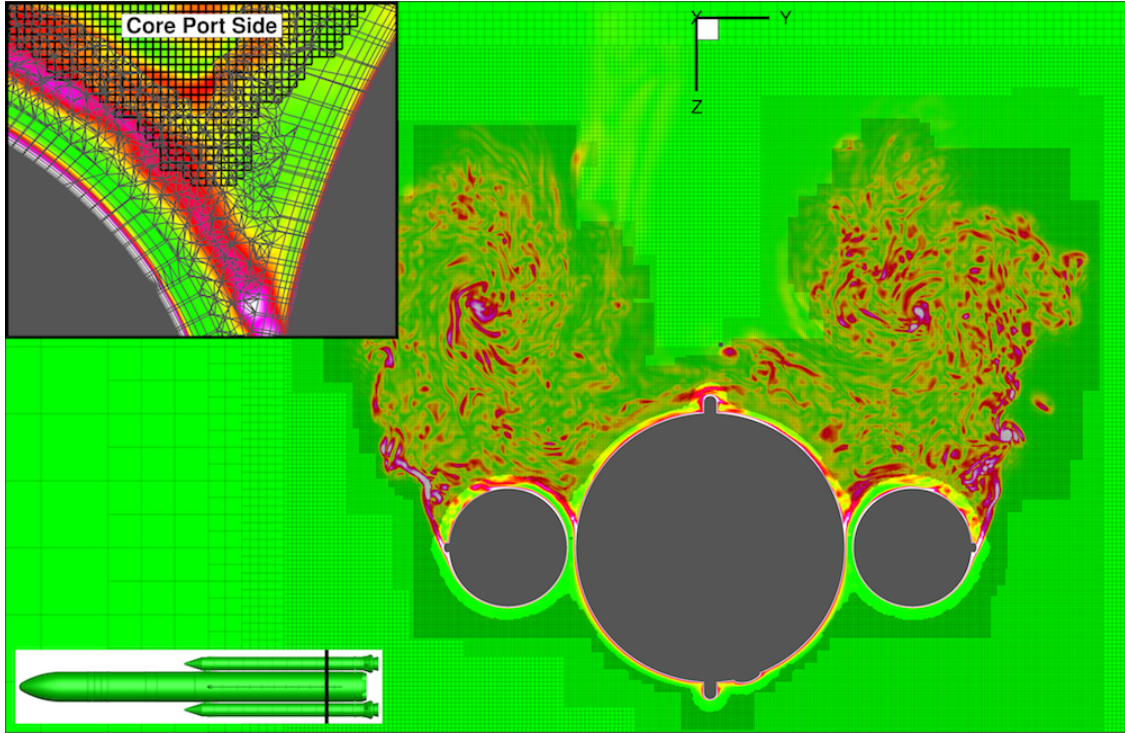
Fig. 14   Kestrel grid slice of the SLS Block 1 configuration at $\alpha_P = 30°$ and $\phi_P = 0°$, with Cartesian AMR based on vorticity magnitude.

of the simulations, the size of the off-body Cartesian grid grows from around 300 million points and levels out at about 1.1 billion points.

The spatial extent of the Cartesian grid solution refinement is specified in the input file; in this case it is set to twice the nominal core diameter off the body of the vehicle in both directions along the Y and Z axes. The Cartesian grid only gets refined in regions where the value of a specified flow field variable exceeds a specified threshold. For the SLS LOT solutions, adaptive mesh refinement was based on the magnitude of the vorticity, with a threshold set at 100; this threshold value corresponds to the yellow contours in the figure. Since the vorticity magnitude is zero upstream of the vehicle, no grid refinement takes place in that region. Extensive refinement occurs on the leeward side of the vehicle, but even there, the adaption method is efficient, as there is little refinement behind the center of the core.

Simulations on the SLS-10003 configuration were conducted with Kestrel version 7.1.2. For both the KCFD and SAMAir codes, simulations were conducted with the SA+DDES turbulence model, inviscid fluxes were discretized with the HLLE++ method, convective fluxes were handled with the Van Leer flux splitting scheme, and the 2nd-order temporal discretization was handled with Gauss-Seidel. The most significant differences between inputs for the two Kestrel flow solvers are that the spatial discretization was 2nd order and the temporal advective damping was set to 0.01 for KCFD, whereas for SAMAir the spatial discretization was 3rd order and the temporal advective damping was set to 0.02. The dimensional time step was set at $\Delta t = 0.0005$ seconds with 3 subiterations per time step and a maximum of 32 sweeps per subiteration. Solution refinements were performed every 250 time steps. The nominal procedure was to run the simulations out 10000 time steps, then run the time-averaging procedure another 4000 time steps. However, the time averaging procedure was occasionally initiated earlier than that if the solution appeared to reach a statistically-steady state sooner, or restarted at 14000 time steps and run another 4000 times steps with time-averaging if the solution required more iterations.

D. Comparison of USM3D, FUN3D, and Kestrel

The relative suitability of the three codes for simulations of the SLS LOT phase of flight was assessed by comparing the results for a pitch sweep at $\phi_P = 0°$. While the correlations between the numerical results and both the wind tunnel force and moment data and wind tunnel pressure port data were crucial, the computational expense of the runs was just

as influential in the selection of the tool for constructing the upcoming databases for the two Block 1B configurations.

The trends seen in comparing results from different formulations of a single solver, where any change in parameters, models, or grids is likely to cause a change in the orientation of the asymmetric vortices and/or the Coanda mode, was also experienced in comparing the selected models for each code. For instance, pressure coefficient results from the three codes and the wind tunnel for the $\alpha_P = 90°$ and $\phi_P = 0°$ are shown in Fig. 15, where the Kestrel SA+DDES result is in red, the FUN3D SA+DDES result is in blue, and the USM3D k-ϵ result is in green.

It is evident that the solution for each flow solver exhibits a different Coanda mode, with the flow through the gaps attaching to both sides of the core for Kestrel, FUN3D capturing the same mode as the wind tunnel with the flow attaching onto the port SRB and starboard side of the core, and USM3D capturing the mode where the flow attaches to both SRBs. The FUN3D model also caught the same orientation of the asymmetric vortex at $\alpha_P = 30°$ and $50°$ as was experienced in the wind tunnel, whereas the Kestrel and USM3D models caught the opposite orientation. However, the phenomena is so sensitive to small perturbations that the Coanda mode exhibited by the solution was not considered as a selection criterion.
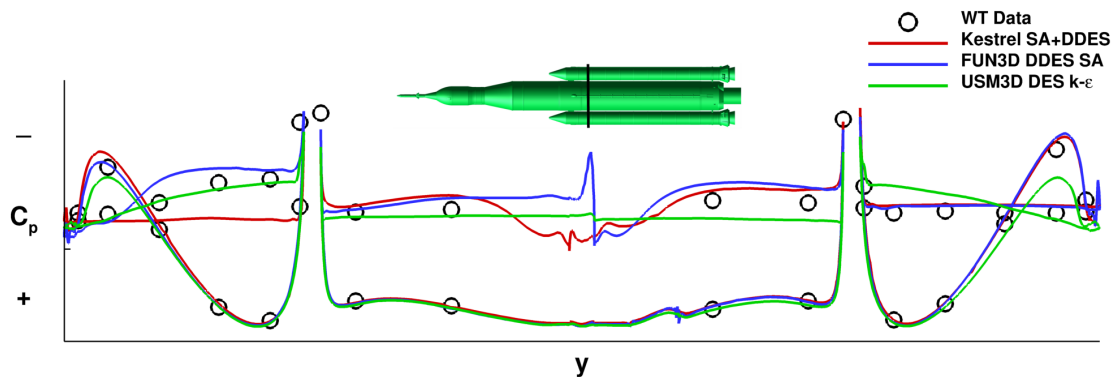

Fig. 15   Pressure coefficient at Station 4 from the wind tunnel and three solvers at $\alpha_P = 90°$ and $\phi_P = 0°$.

In terms of the correlation of the force and moment coefficients between the three codes and the database, the codes were all very consistent in their predictions. For normal force, which is the dominant force at these conditions, predictions from the three codes were within roughly 4% of each other. For side force, all of the codes underpredicted the values relative to the wind tunnel force and moment database values; however, the USM3D and Kestrel values were in good agreement, being within about 5% of each other, while the FUN3D predictions were significantly further away from the force and moment database values. Again, it should be kept in mind that for a more representative comparison of the other two codes to FUN3D, a much finer grid for FUN3D would be required.

The resource requirements for the three flow solvers using the baseline settings, along with a few variants, conformed to expectations and are shown in Table 1. The times listed represent the time required to reach a statistically-steady state and run an appropriate number of additional time-averaging iterations for simulations of the SLS 10003 at LOT conditions using 1200 Haswell processors on the NAS Pleiades cluster. Note that the number of unknowns is proportional to the number of cells for USM3D, the number of nodes for FUN3D, and both the number of nodes (Cartesian grid) and cells (unstructured grid) for Kestrel. The initial USM3D runs were quite slow and even with the improved time marching procedure, the fastest of the USM3D runs came in at about the same amount of time as the slowest of the FUN3D runs. Once again though, taking into consideration that a finer grid is required for FUN3D, then the USM3D and FUN3D computational resource requirements are likely to be fairly equivalent. While it was expected that the incompressible FUN3D model would be faster than the equivalent compressible model, it was quite surprising that runs on the mixed element mesh took 40% more time than runs on the tetrahedral mesh. While the Kestrel runs on NAS delivers solutions two to four times faster than the improved USM3D time stepping procedure, using version 7.1.2 on NAS. Morton and McDaniels at Eglin Air Force Base ran the same problem using version 8 on a DoD cluster and gained another factor of two improvement in speed.

The massive size of the required grids means that Kestrel provides a significant reduction in the time needed for the overall CFD workflow. Unlike the requirement for USM3D and FUN3D, for Kestrel the same near-body grid can be used for every solution, obviating the need for unique unstructured grids for each roll condition. Though FUN3D does have built-in AMR capability, the refinement is performed on an unstructured mesh, making it substantially less computationally efficient than adaption on the Cartesian grid, as employed in Kestrel. Consequently, based on solution

Solver	Cell Type	Nodes (x10^6)	Cells (x10^6)	Turbulence Model	Wall Time (hrs)
USM3D (original Δt)	Tets	78	460	k-ϵ+DES	300-600
USM3D (new Δt)	Tets	78	460	k-ϵ+DES	180-360
FUN3D	Tets	122	717	SA+DDES	135
FUN3D	Mixed	122	717	SA+DDES	189
Kestrel (NAS, version 7)	Mixed	1100	100	SA+DDES	99
Kestrel (Eglin, version 8)	Mixed	1100	100	SA+DDES	46

Table 1   Computational resource requirements for the SLS 10003-DAC2 LOT application.

efficiency, Kestrel was the clear choice as the tool to use for future LOT simulations.

IV. SLS Block 1B Crew (28005) and Cargo (27005)

Based on the lessons learned on the Block 1 Crew configuration, analyses of the Block 1B Crew and Cargo configurations proceeded with Kestrel as the flow solver, running SA+DDES and AMR based on a vorticity magnitude threshold of 100 s^{-1}. The runs for both Block 1B configurations were conducted with version 7.1.2 of Kestrel, rather than version 8, which was available on DoD computer clusters at the time or version 9 which is presently available at the time of this publication. While the increased speed of version 8 or 9 over version 7 would have likely made an improvement on throughput for generating the databases, difficulties arose in implementing the Kestrel near-body off-body methodology on the NAS Pleiades cluster, which have yet to be resolved.

Relative to the DAC2 Block 1 configuration (10003), the Block 1B configuration for analysis (28005) involved a more detailed geometry, included the addition of numerous protuberances. The CFD OML for the SLS-28005 configuration is shown in Fig. 16. The most significant differences are that there are eleven additional rings on each of the SRBs, four additional rings at the top of the core body, and significantly more detail in the representations of the attach brackets, feedlines, and system tunnels. It should be noted that the X locations of the first two Stations of pressure port rings are different from one configuration to another, as they have different geometries forward of the common core stage.
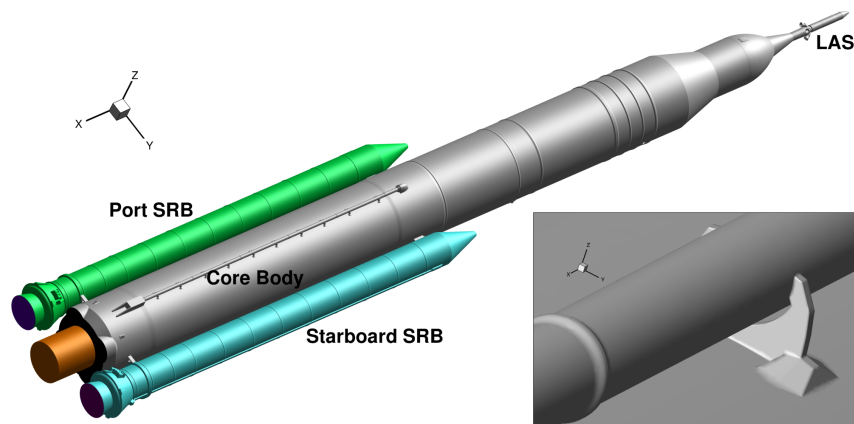

Fig. 16   Block 1B (28005) CFD OML.

An indication of how meticulous the expectation for CFD modeling has become can be gleaned from the bottom-right inset of Fig. 16, which highlights the detail with which the feedline brackets are represented. Given that there are nine brackets on each of the two feed lines, the increase in grid size due to modeling of the brackets is substantial; unfortunately, there were neither the time nor resources to make and run an additional CFD case without the brackets to see if the influence of the brackets could be quantified. Upon merging tets into prisms to create a mixed element grid, then trimming the grid to 24 inches, the size of the SLS-28005 near-body unstructured grid was approximately 120 million cells.

The initial CFD model for the cargo configuration was quite similar to that for the crew configuration, as the lower two thirds of the 27005 OML is identical to that of the 28005 OML. The only difference is that the 27005 model substitutes the cargo payload fairing for the MPCV/LAS of the 28005 model.

A significant change was also made in the wind tunnel methodology between Test 609 for the Block 1 vehicle and Test 633 for the Block 1B vehicles. In Test 633, the decision was made to gain component-level force and moment breakdowns at the cost of pressure information on the SRBs. By installing load cells in both the forward and aft attach brackets for the SRBs, forces and moments on the core and the two SRBs could be distinguished. However, the installation precluded the ability to instrument the pressure ports on the SRBs, so it was no longer possible to discern how well CFD pressure distributions on the SRBs correlated with wind tunnel pressure port values.

A. Kestrel Results for SLS Block 1B Crew (28005)

After the difficulties that were experienced while generating the SLS 10003 database in getting cases through the Pleiades queue, the decision was made to only produce a one quadrant ROM from CFD simulations executed between $\phi_P = 0°$ and 90° for the SLS 28005 database. The single quadrant ROM was then reflected in roll angle to the other three quadrants, then anchored to the wind tunnel force and moment database in all four quadrants to yield the final DFROM. Refinements in selecting the run matrix were also made in an effort to improve over the equally-spaced matrix used for the Block 1 configuration. This involved running RANS simulations at $\alpha_P = 15°$ rather than 10°, then using a design of experiments (DoE) approach to optimize the placement of points for running DDES simulations at total angles of attack greater than 20°. The DoE relied on the use of Block 1 results and wind tunnel data from Block 1B, and focused on maximizing a performance function that sought to achieve CFD force and moment results as close to measured wind tunnel data as possible. The final optimized matrix is shown in Fig. 17.

While RANS solutions were deemed to be sufficient for the lower angles of attack, initial results from the simulations at $\alpha_P = 15°$ did not correlate well with the experimental data, particularly in regard to the leeward surface pressures on the core. In order to resolve the discrepancy, the DDES and AMR modeling that was used at higher angles of attack was used at $\alpha_P = 15°$, but on the RANS grid rather than the DDES grid, with the the AMR limited to three levels of grid refinement. This hybrid method resulted in solutions that were much better correlated with wind tunnel data at little cost, as the Cartesian mesh grew from an initial 120 million points to around 190 million points.

Other than the need to use different grids at lower angles of attack, completion of the SLS-28005 run matrix proceeded smoothly. The AMR was well behaved, with the Cartesian mesh growing from about 300 million points to 1.2 billion points at 30° angle of attack and up to 2 billion points at 90° angle of attack. A sample of the results is shown in Fig. 18, which presents force and moment coefficients from CFD for a pitch sweep at $\phi_P = 0°$, plotted alongside those from the wind tunnel force and moment database. Black squares and error bars indicate the wind-tunnel-generated database values and corresponding uncertainty; note

Fig. 17 Optimal distribution of CFD points from the DoE (for $\alpha_P > 15°$).

that the magnitude of the error between $\alpha_P = 20°$ and 50° is much smaller than for the 10003 database, as the model dynamics of the earlier test were eliminated through the use of a stiffer sting. The error bars on the CFD flow conditions indicate 3σ of the variation of the respective coefficient over the time-averaging window. The agreement between the database and computed values for the normal and side force is very good, and fairly decent for the pitching and yawing moments. It should be noted that the magnitudes of the rolling moment coefficient are very small, as the alpha sweep shown is at zero roll angle. Further, at very high angles of attack (close to 90°), the axial force coefficient is of little consequence.

The most puzzling point is at $\alpha_P = 30°$, for which the computed yawing moment coefficient substantially underpredicts the database value, yet the computed and database values for the side force are quite well aligned. The trend in the database side force values indicates that the orientation of the asymmetric vortex flips from one state to the other between $\alpha_P = 20°$ and 25°, flips again between 30° and 35°, then flips again after 40°.
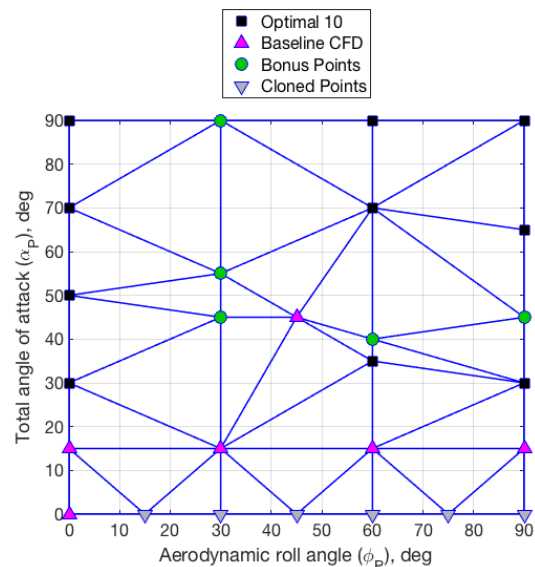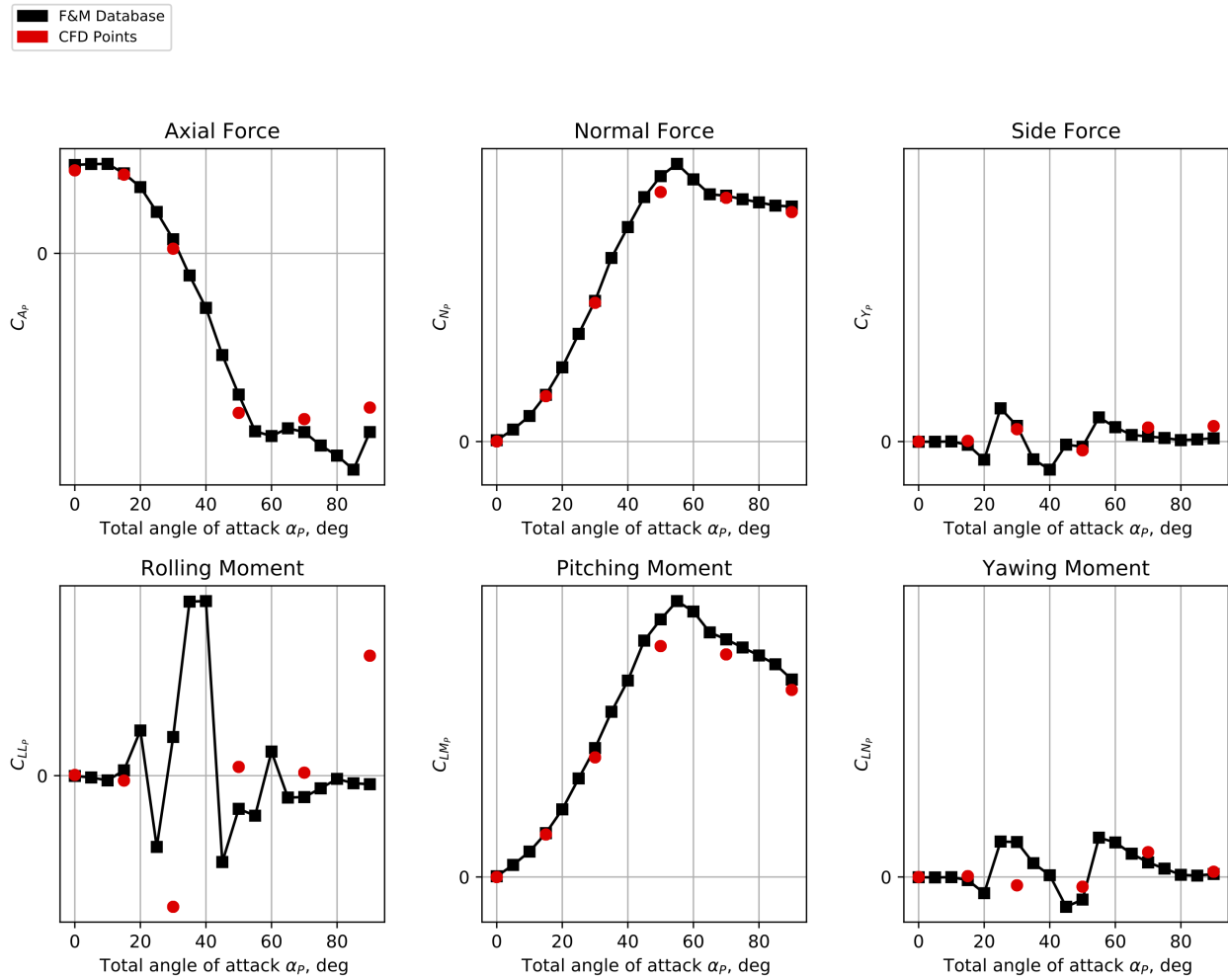
Fig. 18 **SLS-28005 total vehicle force and moment coefficients (missile-axis) from wind tunnel force and moment database and Kestrel CFD, for a pitch sweep at $\phi_P = 0°$.**

Overall, the computed results for the 28005 configuration were well behaved, agreed well with experiment, and used about a quarter of the resources used in simulations for the 10003 database. These metrics represented significant advances in the team's tools, processes, and workflow.

B. Kestrel Results for SLS Block 1B Cargo (27005)

The development of the Transition database for the Block 1B Cargo configuration (SLS-27005) followed the same workflow and process as for the SLS-28005 configuration. The mixed element unstructured grid, trimmed to 24 inches, contained roughly 112 million cells. No changes were made to the DoE matrix, based on comparison of available data.
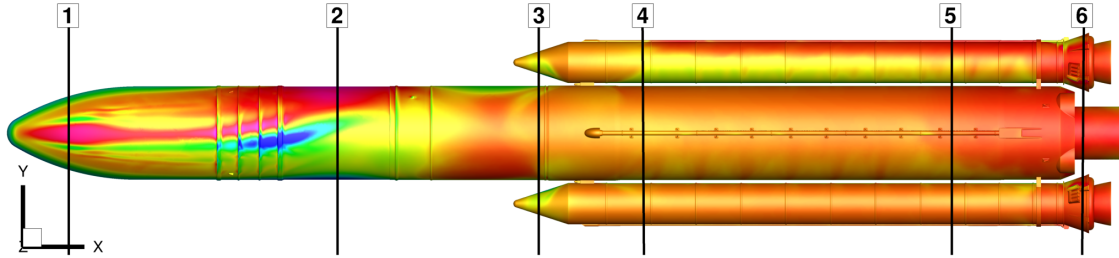

Fig. 19 Pressure coefficient on leeward surface from SA+DDES result at $\alpha_P = 70°$, $\phi_P = 0°$.

While initial CFD simulations were being incorporated into the ROM, it was noticed that CFD solutions at and around $\alpha_P = 70°$ exhibited side force coefficients for which the magnitudes were well beyond what was observed in the force and moment database. Upon closer examination and comparison of surface pressure coefficients relative to those measured in wind tunnel testing, a discrepancy was isolated downstream of the cargo fairing and upstream of the SRBs. The surface pressure coefficient distribution on the leeward side of the vehicle at $\alpha_P = 70°$ and $\phi_P = 0°$ is shown in Fig. 19. A comparison of the computed and wind tunnel pressure coefficient values indicates that the values are in good agreement at Station 1, but the simulation grossly overpredicts the values at Station 2. This comparison allowed the team to isolate the source of the discrepancy to the area forward of Station 2.
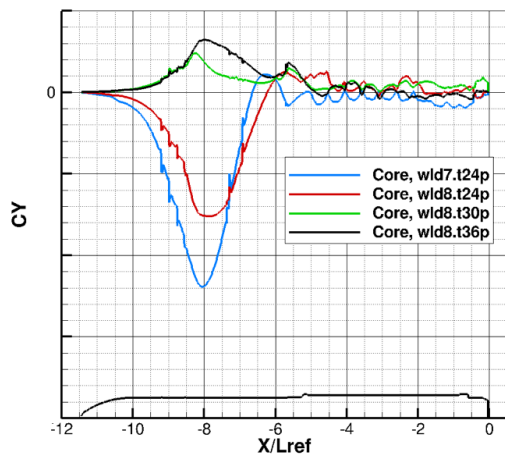

Fig. 20 Sectional side force coefficient lineloads at $\alpha_P = 70°$ and $\phi_P = 0°$ for various near-body grid trim distances.

Initially, the source of the problem was hypothesized to lie in the gridding of the four rings and protuberances ahead of Station 2; however, the grid at these locations appeared satisfactory and the discrepancies persisted even after refinement of the protuberances. For investigation of the anomaly, the team decided to simplify the problem by truncating all geometry aft of the SRB noses from the computational model, but the anomaly could not be recreated in this case, nor when just the SRBs and attach brackets were removed from the model. However, when the attach brackets and noses of the SRBs were reintroduced to the truncated model, the anomaly reappeared. A solution to the problem was found by trying out larger near-body trim distances on this modified truncated geometry.

The original unstructured grid for the SLS-28005 configuration was refined around the four rings and the protuberances in the vicinity of the rings, then trimmed, and simulations were conducted. A plot of the core side force coefficient sectional lineloads for each of the grid trim values is shown in Fig. 20. In this figure, wld7 refers to the baseline refinement level on the protuberances, and wld8 refers to the improved refinement on the protuberances. It can be seen that the magnitude of the asymmetry for the 30-inch and 36-inch trim cases is much less than that of the asymmetry captured in the lower trim cases, and that the directionality of the vortex has switched. Both of these results are more in line with what was observed in wind tunnel testing.

The pressure coefficients for the simulations with trim distances at 24, 30, and 36 inches are shown at the first three

stations for the $\alpha_P = 70°$, $\phi_P = 0°$ case in Fig. 21. It is evident that for the grid trimmed to 24 inches, the computed values are in good agreement with wind tunnel values over the core at Station 1, but are wildly inaccurate at Station 2 and 3, overpredicting the expansion of the leeward side of the vehicle. For the trim distances at 30 and 36 inches, the results at Stations 2 and 3 are in good agreement with each other and fairly good agreement with the wind tunnel results. Simulations were also run for the $\alpha_P = 30°$, $\phi_P = 0°$ case.

Since the results from the 30-inch and 36-inch trim distances were so similar, either could have been chosen for completion of the simulations on the SLS-27005 configuration. Although the choice of 30 inches would have required lower use of computational resources, the choice was made to use the 36-inch trim distance as additional margin, as it would move the nonconservative Overset region between the near-body and off-body grids further away from the vehicle surface and associated flow effects.
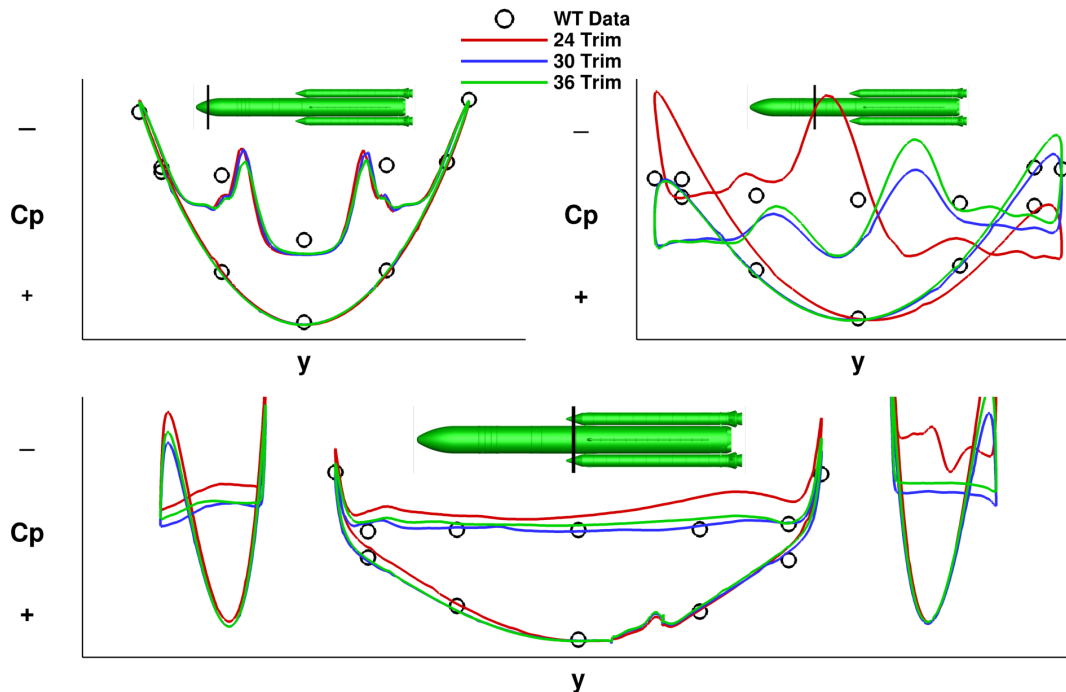

Fig. 21 Pressure coefficient at Stations 1, 2, and 3 from wind tunnel data and Kestrel runs with trim distance of 24 inches (red), 30 inches (blue), and 36 inches (green), at $\alpha_P = 70°$, $\phi_P = 0°$.

The question as to why this problem arose for the SLS-27005 configuration has yet to be definitively resolved. It is conjectured that the problem arises due to interaction effects in the overlap region between the unstructured and Cartesian grids, as the lack of conservation of mass and momentum in the overlap region could cause such flow anomalies. However, in the simplified problems that were tested, the issue did not arise until the noses of the SRBs were included in the simplified situation. So the evidence suggests that defects in the SRB nose grid and Cartesian grid overlap, which are then projected forward to cause inaccuracies in the simulation around the four rings.

Even after problems with the cases at $\alpha_P = 70°$ were addressed through the increase of the near-body grid trim distance to 36 inches, additional difficulties were encountered in the development of an appropriate DFROM for the SLS-27005 database. The trouble arose from the number of cases for which the CFD solutions captured the asymmetric vortex of the opposite orientation than what was observed in the wind tunnel. This led to problems in anchoring the ROM to the wind tunnel database force and moment values, as the DFROM yielded line loads that were implausible.

In response to these challenges, the team expanded CFD matrix to cover all four quadrants, generating missing lineloads information content. This eliminated the need to rotate and reflect solutions, thus reducing the number of multiple core solutions delivered from four to two. Further, the decision was made to unconstrain the DFROM from having to match all wind tunnel nominal force and moment coefficients, and restrict the matching to normal force (CN) and pitching moment coefficient (CLM) in the missile-axis frame. This change resulted in much more physically realistic lineloads as well as a closer match to wind tunnel forces and moments.

The maturation of the tools, processes, and workflow allowed the expansion of the CFD matrix for the Block 1B
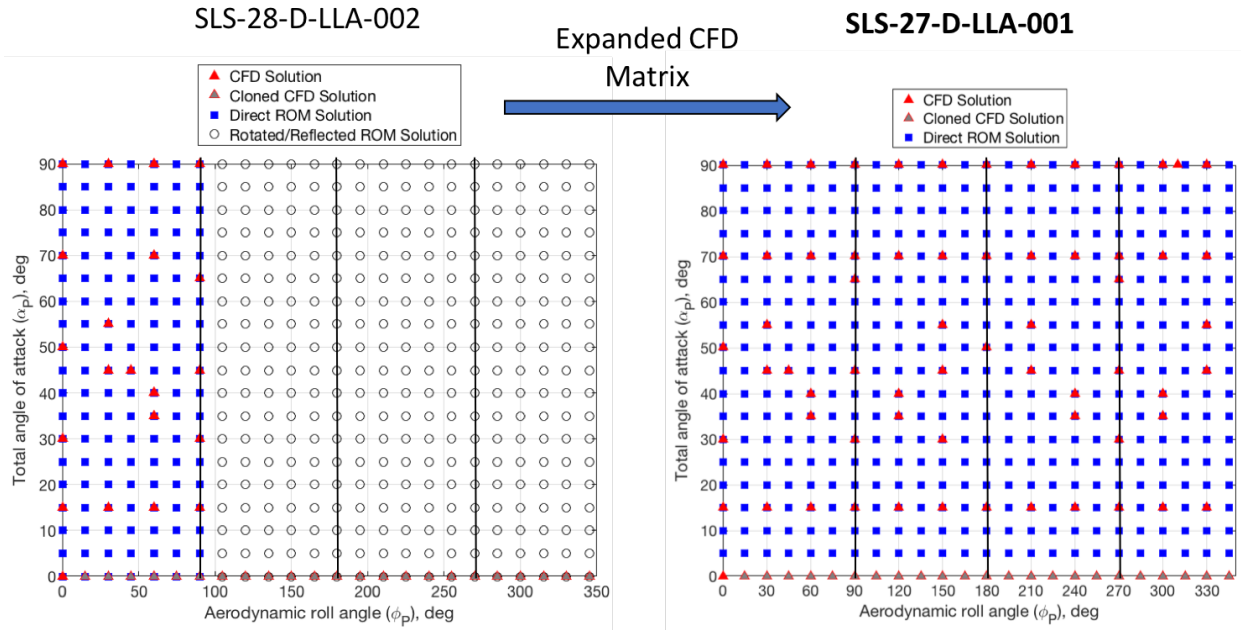
Fig. 22   Effect on delivered databases of expanding CFD capability between 28005 and 27005 analysis cycles.

Cargo vehicle from 21 points in a single quadrant of roll angle to 65 points spanning all four quadrants of roll angle. This expansion in the CFD matrix eliminated the need for the rotation and reflection of ROM solutions, thus resulting in a higher quality database. The difference in data source for each breakpoint is shown graphically in Fig. 22.

Unfortunately, a new anomaly in the CFD solutions arose while running CFD in all four quadrants of roll. Once again the problem that arose at $\alpha_P = 70°$ and $\phi_P = 0°$ now resurfaced at $\phi_P = 270°$. The surface pressure coefficient distribution on the upper side of the vehicle at $\alpha_P = 70°$ and $\phi_P = 270°$ is shown in Fig. 23; the flow direction is from the bottom of the figure to the top.

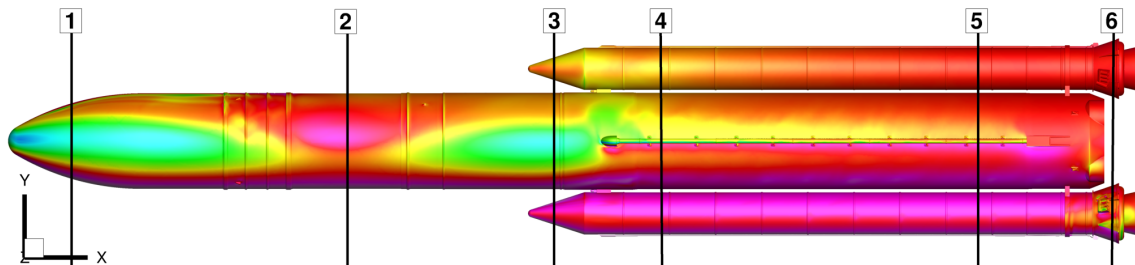**Fig. 23   Pressure distribution on the SLS 27005 surface for the Kestrel run at $\alpha_P = 70°$ and $\phi_P = 270°$.**

Once again, the problem occurs at or near Station 2, propagating downstream to Station 3. This provides a strong indication that the change in trim distance did not address the fundamental weakness of the current gridding strategy. The issue will be revisited for future analysis cycles. Future analysis cycles have moved to a new gridding approach utilizing Heldenpatch/Heldenmesh instead of GTC and VGRID, which preliminary studies have shown could help address gridding deficiencies that have been difficult to overcome using the present set of tools. The significantly decreased turnaround time to generate new grids with Heldenpatch/Heldenmesh alone should enable more rigorous grid studies than have been previously possible, and results of these studies are anticipated to yield further understanding of the impact of the gridding approach on the flowfield solutions for the SLS Liftoff and Transition problem.

V. Conclusions

This report documents some of the reasoning and decisions related to the selection of tools for the LOT problem, along with the evolution of the approach over the course of analyzing multiple SLS configurations. Upon the evaluation of three state-of-the-art CFD flow solvers, the Kestrel solver was selected for use in developing the LOT Lineloads Databases. The selection was due primarily to the significant savings in the CFD solution development turnaround time relative to the workflows for USM3D and FUN3D. The reduction in solution time outweighed the additional time needed to acquire and vet the Kestrel solver. While FUN3D and USM3D do have limited means of adapting the mesh based on the flow using accompanying tools, the built-in, off-body, Cartesian AMR capability in Kestrel was found to be far superior in terms of both usability and computational efficiency.

A turbulence model study showed that the one-equation SA model performed as well as the more computationally expensive two-equation k-ϵ and SST models for this problem. DDES was shown to provide more accurate (closer to wind tunnel) results than RANS, which is expected due to the presence of the large leeward trailing-wake flowfield at such high angles of attack. Thus, the SA model with DDES was chosen for the LOT simulations at higher angles of attack, where massive separation dominates the character of the leeward flow, with RANS solutions being run only for cases at a total angle of attack of 15° or less.

During analysis of the Block 1B Cargo (27005) configuration, grid trim studies showed that significant changes occurred in nominal force coefficients between trim values of 24 inches and 36 inches, but that vortex asymmetry remained generally consistent for trim values between 30 inches and 36 inches. A grid trim value of 36 inches was thus deemed appropriate for the LOT work on the 27005 configuration. This study was prompted by particular challenges specific to the 27005 configuration that can be attributed to the forebody flow asymmetry, which is a general phenomenon observed on all SLS configurations thus far. Prior to this change, a grid trim value of 24 inches was used on the 10003 and 28005 configurations.

Each configuration and analysis cycle brought with it new challenges, but the team has been steadily improving in tools, processes, workflow, and understanding of the aerodynamic complexities unique to the LOT flow regime. While much progress has been made, much work remains to be done. Ongoing work includes efforts toward more rigorous verification and validation of the solutions, including the implementation of grid resolution studies, studying the effect of the difference between flight and wind tunnel Reynolds number, and investigating the effects of alternative flow solver settings. Additionally, new tools and approaches for gridding are being explored which are intended to address many of the possible gridding shortcomings identified in this paper.

References

[1] Sohail, M., Chao, Y., Ullah, R., and Yamin, M., "Computational challenges in high angle of attack flow," *World Academy of Science, Engineering and Technology*, Vol. 80, 2011, pp. 1148–1155.

[2] Fidler, J., and Bateman., M., "Asymmetric Vortex Effects on Missile Configurations," *Journal of Spacecraft and Rockets*, Vol. 12, No. 11, 1975, pp. 674–681.

[3] Hartwich, P., Hall, R., and Hemsch, M., "Navier-Stokes Computations of Vortex Asymmetries Controlled by Small Surface Imperfections," *AIAA 90-0395*, 1990.

[4] Levinsky, E. S., and Yeh, T. T., "An analytical and experimental investigation of circulation control on a circular cylinder by means," *NASA-CR-2114*, 1995.

[5] Capone, F. J., Paulson, Jr., J. W., and Erickson, G. E., "Liftoff and Transition Aerodynamics of the Ares I (A106) Launch Vehicle," *AIAA 2011-997*, 2011.

[6] Krist, S. E., "Kestrel Results at Liftoff Conditions for a Space Launch System Configuration in Proximity to the Launch Tower," *2019 AIAA Aviation Forum*, 2019.

[7] Strelets, M., "Detached Eddy Simulation of Massively Separated Flows," *AIAA 2001-0879*, 2001.

[8] Spalart, P., Deck, S., Shur, M., Squires, K., Strelets, M. K., and Tavin, A., "A new version of detached-eddy simulation, resistant to ambiguous grid densities," *Theoretical Computational Fluid Dynamics*, Vol. 20, No. 181, 2006.

[9] Frink, N. T., Pirzadeh, S. Z., Parikh, P. C., Pandaya, M. J., and Bhat, M., "The NASA Tetrahedral Unstructured Software System (TetrUSS)," *Aeronautical Journal*, Vol. 104, No. 1040, 2000, pp. 491–499.

[10] Biedron, R. T., Carlson, J.-R., Derlaga, J. M., Gnoffo, P. A., Hammond, D. P., Jones, W. T., Kleb, B., Lee-Rausch, E. M., Nielsen, E. J., Park, M. A., Rumsey, C. L., Thomas, J. L., and Wood, W. A., "FUN3D Manual: 13.2," *NASA/TM–2017–219661*, 2017.

[11] Morton, S. A., McDaniel, D. R., Sears, D. R., Tillman, B., and Tuckey, T. R., "Kestrel – A Fixed Wing Virtual Aircraft Product of the CREATE Program," *AIAA 2009-338*, 2009.

[12] Wignall, T., "Liftoff and Transition Database Generation for Launch Vehicles Using Data-Fusion-Based Modeling," *2019 AIAA Aviation Forum*, 2019.

[13] Abdol-Hamid, K. S., Ghaffari, F., and Parlette, E., "Ares I Vehicle Computed Turbulent Ascent Aerodynamic Data Development and Analysis," *Journal of Spacecraft and Rockets*, Vol. 49, No. 4, 2012, pp. 596–608.

[14] NASA Langley Research Center, "TetrUSS: Tetrahedral Unstructured Software System, Publications," , Accessed: March 2018. URL https://tetruss.larc.nasa.gov/tetruss-related-publications/.

[15] Abdol-Hamid, K. S., and Ghaffari, F., "Error Estimates of the Ares I Computed Turbulent Ascent Longitudinal Aerodynamic Analysis," *Journal of Spacecraft and Rockets*, Vol. 49, No. 4, 2012, pp. 609–616.

[16] Krist, S. E., and Ghaffari, F., "Detached Eddy Simulation Results for a Space Launch System Configuration at Liftoff Conditions and Comparison with Experiment," *AIAA 2015-0776*, 2015.